

Broadband nonlinear Hall response and multiple wave mixing in a room temperature altermagnet

Soumya Sankar,^{1,*} Xingkai Cheng,^{1,*} Xinyu Chen,^{1,*} Xizhi Fu,¹ Takahiro Urata,² Wataru Hattori,³ Wenlong Lu,⁴ Zihan Lin,⁴ Dong Chen,⁵ Claudia Felser,⁶ Hiroshi Ikuta,^{3,7} Junzhang Ma,⁴ Junwei Liu,^{1,†} and Berthold Jäck^{1,‡}

¹*Department of Physics, The Hong Kong University of Science and Technology,
Clear Water Bay, Kowloon, Hong Kong SAR*

²*Department of Electrical, Electronic and Computer Engineering,
Gifu University, Gifu, Gifu 501-1193, Japan*

³*Department of Materials Physics, Nagoya University, Nagoya, Aichi 464-8603, Japan*

⁴*Department of Physics, The City University of Hong Kong, Kowloon, Hong Kong SAR*

⁵*College of Physics, Qingdao University, Qingdao 266071, China*

⁶*Max Planck Institute for Chemical Physics of Solids, 01187 Dresden, Germany*

⁷*Research Center for Crystalline Materials Engineering,
Nagoya University, Chikusa-ku, Nagoya, Aichi 464-8603, Japan*

(Dated: September 2025)

Abstract

Crystalline symmetries determine the linear and nonlinear response of materials to external stimuli such as mechanical pressure and electromagnetic fields, governing phenomena such as piezoelectricity, optical activity, and multiple wave mixing with wide ranging technological applications. Altermagnets present a new class of materials with magnetic crystalline order where specific crystal symmetry operations connect anti-ferromagnetic sublattices, leading to non-relativistic spin-splitting of the electronic band structure. Hence, the electric material properties of altermagnets should uniquely mirror these underlying symmetry properties, potentially giving rise to novel phenomena in response to external driving fields. Here, we report the discovery of a broadband third-order nonlinear anomalous Hall effect in altermagnetic CrSb at room temperature. The comparison of our observations with symmetry analyses and model calculations shows that this nonlinear Hall response is induced by the nonlinear electric susceptibility of a Berry curvature quadrupole, which exists within the spin-split band structure of CrSb and is characterized by the underlying crystalline and magnetic symmetries. We then utilize this third-order nonlinear electric susceptibility of CrSb to realize a multiple wave mixing device with pronounced four wave mixing output, which could, in principle, be extended to THz frequencies. Our study discovers that the crystalline magnetic order of altermagnets determines their nonlinear electric material properties, which could facilitate applications in high-frequency electronics, THz generation, communication networks, and energy harvesting.

INTRODUCTION

The response of a material to external stimuli, such as electric and magnetic fields, light, and mechanical pressure, is often described by the susceptibility χ whose properties are governed by the underlying crystalline symmetries. The piezoelectric effect in non-centro-symmetric crystals and circular dichroism of materials with chiral symmetry, as well as multiple wave mixing are examples of linear and nonlinear material responses that lead to wide-ranging technological applications. Altermagnets are a new class of antiferromagnets whose magnetic structure is uniquely connected to crystalline symmetries [1–3]. In conventional antiferromagnets, the spin-up and spin-down lattices are connected by half-translation ($t_{1/2}$) or inversion (\mathcal{P}) symmetry, which guarantees the spin degeneracy of the electronic states in momentum space, as illustrated in Fig. 1(a). In contrast, in altermagnets, crystalline anisotropy results in spatially anisotropic spin-up and spin-down sublattices. These sublattices are connected by rotation or mirror transformations that break $\mathcal{P} \cdot \mathcal{T}$ and $\mathcal{T} \cdot t_{1/2}$ symmetries, where \mathcal{T} denotes the time-reversal symmetry, resulting in non-relativistic spin-splitting of the electronic band structure [4–8], as schematically illustrated in Fig. 1(b). Hence, altermagnetic order can be regarded as a magnetic crystal order that is characterized by the crystalline symmetries and the direction of the magnetic order (Néel) vector [9–12]. Consequently, the presence and specific type of altermagnetic order parameter should in general determine the susceptibility of altermagnets to an external driving field.

It has been proposed that the magnetic crystalline order of altermagnets can support Berry curvature multipoles, arising in the non-relativistic spin-split electronic band structure [13, 14], which can give rise to nonlinear anomalous Hall effects (NLAHE) [15–19]. When the crystalline structure of altermagnets preserves inversion symmetry and the magnetization is compensated $\mathbf{M} = 0$, Berry curvature monopoles (BCM) and dipoles (BCD) are prohibited by symmetry, but a Berry curvature quadrupole (BCQ) can generally appear, as shown in Fig. 1(b). Therefore, altermagnets could exhibit a nonlinear susceptibility $\chi^{3\omega}$ in their material properties induced by a BCQ, potentially giving rise to nonlinear effects, such as the electric third-order NLAHE. This property qualitatively distinguishes altermagnets from \mathcal{PT} -symmetric and \mathcal{P} -breaking antiferromagnets, which cannot exhibit a BCQ on symmetry grounds, as summarized in Fig. 1(a).

Moreover, nonlinear responses of altermagnets as a manifestation of an intrinsic nonlinear susceptibility, such as third-order NLAHE, will exhibit a strong spatial anisotropy, determined by the symmetries of the underlying magnetic crystal order. Hence, they can be qualitatively distinguished from anomalous Hall effects in the linear response that, while prohibited by symmetry in altermag-

nets, could be induced by relativistic spin-orbit coupling [20–24]. To date, concepts to utilize the spin-split band structure of altermagnets mostly focus on spintronic applications that remain limited to materials with d –wave order parameter by symmetry constraints [25–32]. Therefore, experimental insight into the general impact of the non-relativistic spin splitting on the linear and non-linear electric material properties of altermagnets will be critical to advance our fundamental knowledge and identify technological application scenarios of this new class of magnetic materials.

In this work, we provide experimental evidence for a broadband nonlinear anomalous Hall response in a room temperature altermagnet. Conducting electric Hall effect measurements of altermagnetic CrSb along different spatial directions, we detect a distinct third-order NLAHE. The comparison with symmetry analyses and model calculations makes a compelling case that this effect is induced by a Berry curvature quadrupole, which exists within the non-relativistic spin-split electronic band structure in a perfect altermagnet without any additional net magnetic moment. We also show that the broadband nonlinear susceptibility $\chi^{3\omega}$ of CrSb can be utilized to realize a multiple wave mixing device at room temperature, expanding the potential application scope of altermagnets beyond spintronics to high-frequency electronics, communication networks, and energy harvesting [33].

SYMMETRY PROPERTIES OF ALTERMAGNETIC ORDER IN CrSb

CrSb crystallizes in a hexagonal lattice structure ($a = 4.12\text{ \AA}$, $c = 5.47\text{ \AA}$, $P6_3/mmc$ space group) [34]. Its antiferromagnetic structure can be characterized by an A-type Néel vector whose easy axis points along the crystallographic c –axis [35, 36], as seen in Fig. 1(c). In this configuration, the magnetic moments of Cr pointing along the c –axis are aligned in parallel within the hexagonal Cr layer and antiparallel between two neighboring layers. For simplicity, we define a Cartesian coordinate system in which the x , y , z directions correspond to the crystallographic $[2\bar{1}\bar{1}0]$, $[01\bar{1}0]$, and $[0001]$ directions, respectively. In the absence of relativistic spin-orbit coupling (SOC), which is generally weak for Cr 3d electrons, the magnetic structure of CrSb can be described by spin-group formalism [3, 37–41]. Within this notation, the spin sublattices of CrSb are connected by two symmetry operations $C_2^s M_z$ and $C_2^s \tilde{C}_{6z}$, where C_2^s , M_z , and $\tilde{C}_{6z} = C_{6z} t_{1/2}$ denote a spin-flip operation, mirror-z operation, and six-fold out-of-plane rotation C_{6z} combined with a half-translation $t_{1/2}$ along $[0001]$, as schematically illustrated in Fig. 1(d). Hence, CrSb can be classified as a bulk g -wave altermagnet [3] whose magnetic structure breaks $\mathcal{P} \cdot \mathcal{T}$ and $\mathcal{T} \cdot t_{1/2}$. The breaking of these combined symmetries manifests in non-relativistic spin-splitting of the electronic states in

momentum space [5, 6, 42, 43], a characteristic feature of altermagnetism.

We visualize this momentum-space splitting of the electronic bandstructure of CrSb by conducting angle-resolved photo-electron spectroscopy (ARPES) measurements on the surface of cleaved bulk crystals (see Methods section for details). The symmetry transformation $C_2^s M_z$ and $C_2^s \tilde{C}_{6z}$ between the spin sublattices manifest in nodal planes of spin-degenerate bands along high-symmetry directions and planes [3, 42]. Therefore, to visualize the spin-split band structure, we have performed a spectroscopic cut away from high-symmetry lines at $k_y = 3.3^{-1}$ and $k_z = 1.2^{-1}$ along a direction parallel to $\Gamma - K$ (see Sec. I for details of the cut location within the xy -plane of the Brillouin zone). The resulting energy-dependent ARPES signal is shown in Fig. 1(e). As can be seen, our experimentally detected signal is in good agreement with the spin-split electronic band structure obtained from DFT calculations, which is overlaid to the data (see Methods section for details). We detect the non-relativistic band splitting of the bands down to 0.2 eV below Fermi energy, consistent with recently published results [5, 6, 42, 43].

In the next step, we derive a qualitative understanding of the linear ($n = 1$) and nonlinear ($n > 1$) current responses $\mathbf{j}^{n\omega} = \sigma^{n\omega}(\mathbf{E}^\omega)^n$ of CrSb to the application of an a.c. external electric field \mathbf{E}^ω of frequency ω . These responses are determined by the linear and nonlinear electric conductivity tensors $\sigma^{n\omega}$. In simple terms, $\sigma^{n\omega}$ accounts for electric material properties, such as the electric resistivity and the electric Hall effect. Interestingly, the quantum-geometric tensor \mathcal{Q} of the electronic wavefunction, which is determined by all crystalline and magnetic material symmetries, can also contribute to $\sigma^{n\omega}$ [44–46]. The Berry curvature $\boldsymbol{\Omega}$, which corresponds to the imaginary part of \mathcal{Q} , can contribute to off-diagonal elements and manifest in the observation of linear and nonlinear anomalous Hall effects. The quantum metric, which corresponds to the real part of \mathcal{Q} , can generally contribute to all tensor elements of the nonlinear conductivity tensors ($n > 1$) and give rise to both longitudinal and transverse responses. Note that the quantum metric does not contribute to the linear conductivity tensor $\sigma^{1\omega}$.

We can derive specific contribution of \mathcal{Q} to the tensor elements of $\sigma^{n\omega}$ for $n \geq 1$ in CrSb by conducting a symmetry analysis. Details of the symmetry analysis are shown in Sect. II of the Suppl. Materials and summarized in Fig. 2(a). The altermagnetic structure of CrSb breaks the combined $\mathcal{P} \cdot \mathcal{T}$ symmetry and generally allows for a finite $\boldsymbol{\Omega}$ in the Brillouin zone. However, when spin-orbit coupling is weak, CrSb exhibits compensated magnetization $\mathbf{M} = 0$ and thus preserves $C_2^s M_z$ and $C_2^s \tilde{C}_{6z}$ symmetry. This will force integration of $\boldsymbol{\Omega}$ over the Brillouin zone to vanish and lead to the absence of the first-order anomalous Hall conductivity, $\sigma_{\beta\alpha}^{1\omega}$, where α and β denote spatial directions that are perpendicular to each other and lie within one plane. Therefore, by symmetry

arguments, $\sigma_{\beta\alpha}^{1\omega} = 0$ and altermagnets do not exhibit an intrinsic first-order anomalous Hall effect (AHE) induced by the non-relativistic spin-splitting of the electronic structure. Regarding the second order nonlinear conductivity tensor $\sigma_{2\omega}$, Berry curvature and quantum-metric contributions require broken \mathcal{P} . However, the centro-symmetric lattice structure of CrSb preserves \mathcal{P} , and hence $\sigma^{2\omega} = 0$ and CrSb are expected to exhibit no longitudinal or transverse second-order response.

Unlike the first- and second-order responses, our analyses show that the magnetic crystal order of CrSb does support a BCQ and a nonlinear third-order response. Specifically, we find that only one quadrupole Q_{xxxx} exists, which lies within the xz -plane of the Brillouin zone, and contributes to exactly one off-diagonal component $\sigma_{xxxx}^{3\omega}$ of the third-order conductivity tensor, as seen in Fig. 2(a). Hence, CrSb should exhibit a third-order nonlinear susceptibility χ_{xxxx} , which can give rise to a third-order NLAHE induced by a BCQ when an a.c. current of frequency ω is applied along the x -direction of the crystal. This NLAHE would manifest as a finite transverse voltage response $V_{xxxx}^{3\omega}$ at the third harmonic 3ω along the z -direction. Critically, owing to the anisotropic nature of the BCQ distribution in the Brillouin zone, CrSb should not exhibit a third-order Hall response when the current is applied along the y - or z -directions, that is, $V_{yy}^{3\omega} = 0$ and $V_{zz}^{3\omega} = 0$, respectively. Meanwhile, other potential contributions to $\sigma_{xxxx}^{3\omega}$, such as quantum metric and Drude effects, are forbidden by the crystal symmetry of CrSb.

The absence of first- and second-order responses and the predicted third-order nonlinear susceptibility $\chi^{3\omega}$ of CrSb represent unique intrinsic properties of altermagnetic order in the non-relativistic limit and the spatial anisotropy of $\chi^{3\omega}$ precisely reflects the magnetic and crystalline symmetries encoded in the altermagnetic g-wave order parameter of CrSb [3]. Finally, also note that our symmetry analysis also shows that CrSb can host quantum metric quadrupoles (QMQ), which contribute to the diagonal-elements $\sigma_{\alpha\alpha\alpha\alpha}^{3\omega}$, that is, the longitudinal voltage responses along all crystallographic directions, as summarized in Fig. 2(a). Critically, the presence of finite QMQ tensor elements does not have specific symmetry requirements. Hence, QMQ-induced longitudinal voltage responses are not a distinguishing feature of altermagnets as they can generally appear in all magnetic configurations (ferromagnetic, antiferromagnetic, altermagnetic, and non-magnetic).

OBSERVATION OF THE THIRD-ORDER NLAHE AT ROOM TEMPERATURE

We have fabricated Hall bar devices to test the presence of the predicted third-order Hall response of altermagnetic CrSb to an external electric driving field. To this end, we have used focused ion beam (FIB) method to cut $1\ \mu\text{m}$ thin rectangular-shaped lamellae from a prism-shaped CrSb bulk

crystal, which has a hexagonal cross section, as shown in Fig. 2(b). Following our symmetry analysis, lamellae were cut within the xz -, yz -, and zx -planes of the CrSb crystal to examine the anisotropic nature of the third-order Hall response. The resulting device samples are labeled ' XZ' , ' YZ' , and ' ZX' . In the next step, the lamellae were placed on prepatterned gold electrodes, and electric contact between the lamellae and gold electrodes was established via FIB-deposited platinum (see Methods section for device fabrication details). Fig. 2(c) shows a scanning-electron microscopy (SEM) image of the ' XZ' device; SEM images of all other devices are shown in Sec. III of the Suppl. Materials. Note that we obtain ' XZ' and ' ZX' devices by rotating one of the crystalline lamellae by 90° before placing it on the electrodes.

We now focus on measurements of the nonlinear electric response of CrSb in a current-biased measurement geometry. We apply a sinusoidal a.c. excitation current of frequency 1ω along the α direction and record the longitudinal $V_{\alpha\alpha\alpha\alpha}^{3\omega}$ and transverse $V_{\beta\alpha\alpha\alpha}^{3\omega}$ third-order voltage responses at the third harmonic 3ω using lock-in measurements. The data and detailed analysis of the longitudinal third-response are presented in Sec. IV of the Suppl. Materials. In Fig. 2, (d)-(f) we schematically illustrate the specific measurement geometry of the ' XZ' ', ' ZX' ', and ' YZ' devices respectively. For example, when a bias current is applied along the x -direction of the ' XZ' cut in Fig. 2(d), the longitudinal and transverse third-order voltage responses correspond to $V_{xxxx}^{3\omega}$ and $V_{zxxx}^{3\omega}$, respectively. As can be seen, the choice of samples ' XZ' ', ' YZ' ', and ' ZX' enables us to examine the nonlinear electric response of CrSb when the a.c. current bias is applied along the x -, y -, and z -directions of the crystal. Control experiments that confirm the accuracy of our lock-in detection scheme are presented in Sec. V of the Suppl. Materials.

In Fig. 2(g)-(i), we display the transverse third-order voltage response $V_{\beta\alpha\alpha\alpha}^{3\omega}$ recorded on Hall bar devices ' XZ' ', ' ZX' ', and ' YZ' at room temperature as a function of the cubed applied bias current. Our measurements show that the ' XZ' ' device exhibits a distinct $V_{zxxx}^{3\omega}$ signal and $V_{zxxx}^{3\omega}$ scales cubically with the bias current (see linear fit as black dashed line). This establishes $V_{zxxx}^{3\omega}$ as a third-order NLAHE. Interestingly, the detection of the NLAHE is highly anisotropic. Measurements conducted on the ' ZX' ' and the ' YZ' ' devices do not detect signatures of a third-order Hall effect, as seen in Fig. 2, (h) and (i). The observation of the NLAHE in the ' XZ' ' device presents the key result of our work, and is reproduced on another device ' $XZ2$ ', as shown in Ext. Data Fig. 1. The distinct spatial anisotropy of this measurement signal is in excellent agreement with results of our symmetry analysis, summarized in Fig. 2(a), suggesting that $V_{zxxx}^{3\omega}$ is induced by a Berry curvature quadrupole Q_{xxxx} within the spin-split band structure of CrSb.

We have also characterized the first and second order transverse voltage responses. Our mea-

surements, presented in Sec. VI of the Suppl. Materials, show that none of the devices exhibits a longitudinal ($V_{\alpha\alpha\alpha}^{2\omega}$) or transverse ($V_{\beta\alpha\alpha}^{2\omega}$) second-order voltage response that scales quadratically with the applied bias current. This finding is consistent with results from our symmetry analysis and the general understanding that CrSb does not break \mathcal{P} . However, we detect a small transverse first-order voltage $V_{\beta\alpha}^{1\omega}$ in all devices. This observation is unexpected because our preceding analysis shows that the symmetries of CrSb prohibit the appearance of a Hall effect. Magnetic field B dependent measurements, shown in Sec. VI of the Suppl. Materials, reveal that $V_{\beta\alpha}^{1\omega}$ is symmetric with respect to the reversal of the B -field direction, suggesting that this signal arises from anisotropy effects rather than being a true Hall signal. Indeed, an extended symmetry analysis, presented in Sec. VII of the Suppl. Materials, confirms that this first-order signal most likely arises from small angular misalignments of the sample plane with the principal crystallographic axes. Such small angular misalignment is a consequence of the alignment accuracy of about 0.5° of the CrSb bulk crystal in the FIB cutting process (see Methods section).

EXPERIMENTAL CHARACTERIZATION OF THE THIRD-ORDER NLAHE IN CRSB

The results of our symmetry analysis suggest that the experimentally detected third-order NLAHE in device ' XZ' is induced by a BCQ that exists within the xz -plane of the Brillouin zone. At the same time, other mechanisms such as skew scattering [47, 48], a longitudinal third-order Drude response [46], Joule heating [49], and an out-of-plane magnetization can also contribute or give rise to a third order transverse voltage. To strengthen the causality between the observed third-order NLAHE and a BCQ supported by the non-relativistic spin-split band structure, we have conducted further magnetic field and temperature dependent measurements.

Like conventional antiferromagnets, altermagnets have a compensated magnetization $\mathbf{M} = 0$. However, relativistic spin-orbit coupling could theoretically give rise to a small out-of-plane magnetization M_z resulting in an anomalous contribution to the Hall effect [24]. Moreover, Joule heating could cause a longitudinal third-order voltage [49], which in the presence of a small net magnetization M_z could give rise to a third-order NLAHE. The amplitude of these contributions can be generally tuned using an external magnetic field B_z because $M_z \propto B_z$. Therefore, to exclude scenarios in which the third-order NLAHE would be caused by a net magnetization or Joule heating, we have studied the dependence of $V_{zxxx}^{3\omega}$ on an external magnetic field applied along the out-of-plane direction (y -axis for the ' XZ' device). As shown in Fig. 3(a), $V_{zxxx}^{3\omega}$ is finite at $B = 0$ and remains unchanged for magnetic field sweeps between -40 kOe and 40 kOe. This observation suggests that

$V_{zxxx}^{3\omega}$ is not induced by a net magnetization or Joule heating that would couple to \mathbf{B} but rather represents an intrinsic nonlinear material response to a longitudinal a.c. current drive.

Next, we examine the temperature (T)-evolution of the third-order NLAHE. In general, different mechanisms, such as skew scattering and BCQ, can contribute to the measurement signal $V_{zxxx}^{3\omega}$. Critically, each of these mechanisms is characterized by a distinct dependence on the charge carrier scattering time τ , which is generally temperature dependent. Therefore, a scaling law analysis in terms of τ can be used to extract their respective contributions to $V_{zxxx}^{3\omega}$. To this end, we record the longitudinal first-order $\sigma_{xx}^{1\omega}(T)$ and third-order nonlinear anomalous Hall conductivity $\sigma_{zxxx}^{3\omega}(T)$ as a function of temperature T between room temperature ($T = 300$ K) and 150 K. As seen in Fig. 3(b), $\sigma_{xx}^{1\omega}(T)$ monotonically increases toward lower temperatures, consistent with the metallic character of CrSb. In contrast, $\sigma_{zxxx}^{3\omega}(T)$ reduces by about a factor of two over the same temperature range. Note that lowering the temperature even further resulted in contact degradation caused by thermal stress for all CrSb devices that we had fabricated, and the effect of this degradation was strong for $\sigma_{zxxx}^{3\omega}(T)$; this currently prevents us from examining $V_{zxxx}^{3\omega}$ over an even larger temperature range.

To conduct a scaling law analysis, we plot $E_{zxxx}^{3\omega}/(\sigma_{xx}^{1\omega}(E_{xx}^{1\omega})^3)$ as a function of the squared longitudinal conductivity in Fig. 3(c). $E_{zxxx}^{3\omega}$ and $E_{xx}^{1\omega}$ denote the electric field amplitudes of $V_{zxxx}^{3\omega}$ and $V_{xx}^{1\omega}$, respectively. It was previously shown that BCQ contributions β to the third-order transverse voltage can be determined using the scaling law $E_{zxxx}^{3\omega}/(\sigma_{xx}^{1\omega}(E_{xx}^{1\omega})^3) = \alpha\sigma_{xx}^2 + \beta$, where α accounts for contributions from skew scattering and BCQ contributions can be identified and extracted from the vertical intercept [19]. We can fit the data using this scaling law expression, as seen in Fig. 3(c). The finite vertical intercept $\beta = (-9.77 \pm 0.07) \times 10^3 \Omega \mu\text{m}^3 \text{V}^{-2}$, extracted from the fit, supports a BCQ-induced third-order NLAHE that accounts for $\approx 70\%$ of the detected $V_{zxxx}^{3\omega}$ amplitude at room temperature, while the linear term $\alpha = (1032 \pm 8) \times 10^{-6} \Omega^3 \mu\text{m}^5 \text{V}^{-2}$ indicates the presence of skew-scattering contributions that become more dominant at lower temperatures. Therefore, the scaling law analysis of $V_{zxxx}^{3\omega}$ is consistent with the results of our symmetry analysis, suggesting the observation of a BCQ-induced third-order NLAHE. Note that a comparable analysis of the longitudinal third-order voltages, presented in Sec. IV of the Suppl. Materials, reveals that $V_{\alpha,\alpha,\alpha,\alpha}^{3\omega}$ is dominated by contributions from a QMQ and Drude scattering, which is consistent with our symmetry analysis presented in Fig. 2(a).

BERRY CURVATURE QUADRUPOLE IN THE SPIN-SPLIT BAND STRUCTURE OF CrSb

We further present results from density functional theory (DFT) calculations to validate that the electronic band structure of CrSb supports a BCQ within xz -plane of the Brillouin zone. Calculation details are presented in the Methods section. In the absence of relativistic SOC, spin remains a good quantum number, and spin-splitting in the electronic band structure of CrSb is induced by non-relativistic antiferromagnetic exchange energy. This process results in numerous band crossing points of opposite-spin polarization near the Fermi energy. Introducing SOC lifts these band degeneracy points, whose small spectral gaps act as Berry curvature hotspots near Fermi energy, as seen in Fig. 3(d).

To understand the impact of these hotspots on the nonlinear third-order susceptibility of CrSb, we consider the projection of the electronic states into the relevant crystallographic direction. According to our magnetic point group analysis (see Sec. II of the Suppl. Mat.), the combined crystalline and magnetic symmetries support exactly one BCQ tensor element \mathcal{Q}_{xxxx} within the xz -plane of the crystal, which would give rise to the observed third-order NLAHE $V_{xxxx}^{3\omega}$. To validate this understanding in terms of the realistic band structure, we plot the Fermi surface overlaid with the second derivative $\mathcal{Q}_{xxxx}(k_x, k_z) = \partial_x \partial_z \Omega_{xz}$ of the Berry curvature Ω_{xz} within the xz -plane of the Brillouin zone, as shown in Fig. 3(e). As can be seen, the band structure of CrSb supports a distinct BCQ distribution within the xz -plane, whose momentum-space characteristics are determined by the underlying crystalline and magnetic symmetries. An extended symmetry analysis of the BCQ distribution in the Brillouin zone is presented in Sec. VIII of the Suppl. Materials. Critically, we also find that the momentum space integration of $\mathcal{Q}_{xxxx}(k_x, k_z)$ results in a finite contribution to $\sigma_{xxxx}^{3\omega}$ at Fermi energy, as seen in Ext.Data.Fig. 2. Hence, consistent with results from our symmetry and scaling law analyses, our band structure analysis suggests that the spin-split electronic bands of CrSb support a BCQ-induced third-order NLAHE.

Note that experimentally determined and theoretical values of the linear anomalous Hall conductivity are often quantitatively compared to support the interpretation of the experimental observations [50, 51]. In the case of BCQ, we point out that such comparison is generally challenging. Owing to the $E_{xxxx}^{3\omega}/(\sigma_{xx}^{1\omega}(E_{xx}^{1\omega})^3)$ form of the scaling law [19], the extracted BCQ contribution to $\sigma_{xxxx}^{3\omega}$ is a function of $\sigma_{xx}^{1\omega}$, where $E_{xx}^{1\omega} \propto (\sigma_{xx}^{1\omega})^{-1}$. Hence, the extracted BCQ value is influenced by various material properties, such as charge carrier density and electron mobility, determined by the details of the electronic band structure, impurity concentration, and temperature, effects that

are not included in the calculation of the BCQ using a Boltzmann equation approach based on a DFT-derived tight-binding model, making a quantitative comparison very challenging.

ROOM TEMPERATURE MULTIPLE WAVE MIXING IN AN ALTERMAGNET

Our combined experimental and theoretical study provides evidence for a BCQ induced third-order NLAHE in altermagnetic CrSb. In general, NLAHEs hold promise for technological applications in the field of high-frequency signal generation, conversion, and rectification, as well as energy harvesting of ambient RF signals [33]. To quantify the potential of altermagnets in this context, we first consider the third-order nonlinear susceptibility $\chi_{xxxx}^{3\omega}$ of the BCQ. It can be derived from the Boltzmann equation and is typically of the form

$$\chi_{xxxx}^{3\omega} \propto \frac{Q_{xxxx}}{(1 - i\omega\tau)(1 - 2i\omega\tau)(1 - 3i\omega\tau)} \quad (1)$$

and captures the inertia of the BCQ in response to an external driving field. It follows that the bandwidth of the third-order nonlinear Hall response is limited by the charge carrier relaxation time $\tau = \mu m_{\text{eff}}/e$, where μ , m_{eff} , and e denote the charge carrier mobility, effective mass, and electron charge, respectively. Using experimentally determined values of μ and m_{eff} for CrSb [52], we estimate $\tau \approx 1 \text{ ps}$. This time scale corresponds to the maximum bandwidth $\delta f = 1/\tau \approx 1 \text{ THz}$ of $\chi_{xxxx}^{3\omega}$. To experimentally test the bandwidth of the NLAHE in CrSb, we have recorded the amplitude of $V_{xxxx}^{3\omega}$ as a function of the frequency ω of the longitudinal a.c. drive current I_x . As can be seen in the inset of Fig. 4(a), $V_{xxxx}^{3\omega}$ remains constant over the entire experimentally accessible frequency range $f \leq 100 \text{ kHz}$. These broadband characteristics of the NLAHE in CrSb are consistent with our above estimate for $\chi_{xxxx}^{3\omega}$.

Finally, we utilize this nonlinear electric response of altermagnetic CrSb to realize a broadband multiple wave mixing (MWM) device. MWM can occur in materials with a third-order nonlinear susceptibility $\chi^{3\omega}$ and describes the combination of several input electromagnetic waves into output waves of different frequency. This phenomenon is widely used to realize coherent tunable light sources in parametric oscillators, in quantum-limited amplification, and communication networks and high-resolution spectroscopy. While MWM is typically realized using the nonlinearity of atoms and superconducting circuits [53–55], more recent studies also discuss this phenomenon in the context of nonlinear Hall effects [56, 57]. Here, we show that MWM can be realized in altermagnets using the $\chi_{xxxx}^{3\omega}$ of the BCQ in CrSb.

We implement a MWM device by connecting two current sources $I_x^{1\omega_1}$ and $I_x^{1\omega_2}$ with identical

current amplitude but different frequencies ω_1 and ω_2 in parallel along the longitudinal direction of device 'XZ', as shown in the inset of Fig. 4. We then record the frequency spectrum of $V_{zxxx}(f)$. When two alternating currents with $\omega_1 = 125$ Hz and $\omega_2 = 33$ Hz are applied, our measurements show that $V_{zxxx}(f)$ exhibits about 20 pronounced spectral peaks between 0 to 500 Hz, as seen in Fig. 4(a). In addition to the fundamental (ω_1 and ω_2) and third harmonic ($3\omega_1$ and $3\omega_2$) frequencies of the input signals, we also detect spectral components that result from sum frequency generation (SFG, $\omega_1 + \omega_2$) and different frequency generation (DFG, $\omega_1 - \omega_2$) as well as MWM of the input signals. The MWM output appears at frequencies $\omega = \alpha\omega_1 \pm \beta\omega_2$ where α and β are positive integers. We find that the four wave mixing (4WM) signals $V_{zxxx}^{2\omega_1 \pm \omega_2}$ at $\omega = 2\omega_1 - \omega_2 = 217$ Hz and $\omega = 2\omega_1 + \omega_2 = 283$ Hz exhibit the largest output amplitude next to the fundamental harmonics ω_1 and ω_2 . Critically, the occurrence of 4WM in a nonlinear medium requires a finite third-order nonlinear susceptibility, which here is provided by $\chi_{zxxxz}^{3\omega}$ of the Berry curvature quadrupole. We have also conducted a control experiment by replacing the 'XZ' device with a simple resistor of electric resistance $R = 100 \Omega$. Repeating the same measurement as before, we find that the transverse output signal does not exhibit SFG, DFG, and MWM components, as seen in Fig. 4(b). Only small spectral peaks can be detected at the fundamental frequencies ω_1 and ω_2 , which arise from inductive coupling in the measurement circuit. These results establish the realization of a broadband multiple wave mixing device based on the intrinsic nonlinear susceptibility of CrSb.

To conclude, our discovery of a Berry curvature quadrupole induced NLAHE in the paradigmatic altermagnet CrSb experimentally establishes that the intrinsic electric response of fully compensated altermagnets [13, 14] is governed by the underlying magnetic crystal order [10, 11]. Hence, our study provides a generalized understanding of the impact of the non-relativistic spin splitting band structure on the electric material properties of altermagnets beyond the linear response regime previously studied in the limit of relativistic spin-orbit coupling and finite magnetization [20–24]. Existing concepts for the potential use of altermagnets in spintronics applications are confined to *d*-wave altermagnets owing to symmetry-constraints [25–32]. Through the realization of broadband multiple wave mixing device, which utilizes the nonlinear susceptibility $\chi^{3\omega}$ of the Berry curvature quadrupole embedded in the spin-split electronic structure of CrSb, our study overcomes these limitations and showcases the general potential of (*d*, *g*, *i*)–wave altermagnets in applications for high-frequency electronics, THz generation, communication networks, and energy harvesting.

* These authors contributed equally.

† liuj@ust.hk

‡ bjaeck@ust.hk

- [1] S. Hayami, Y. Yanagi, and H. Kusunose, *Physical Review B* **102**, 144441 (2020).
- [2] H.-Y. Ma, M. Hu, N. Li, J. Liu, W. Yao, J.-F. Jia, and J. Liu, *Nature communications* **12**, 2846 (2021).
- [3] L. Šmejkal, J. Sinova, and T. Jungwirth, *Physical Review X* **12**, 031042 (2022).
- [4] J. Krempaský, L. Šmejkal, S. D'souza, M. Hajlaoui, G. Springholz, K. Uhlířová, F. Alarab, P. Constantinou, V. Strocov, D. Usanov, *et al.*, *Nature* **626**, 517 (2024).
- [5] J. Ding, Z. Jiang, X. Chen, Z. Tao, Z. Liu, T. Li, J. Liu, J. Sun, J. Cheng, J. Liu, *et al.*, *Physical Review Letters* **133**, 206401 (2024).
- [6] S. Reimers, L. Odenbreit, L. Šmejkal, V. N. Strocov, P. Constantinou, A. B. Hellenes, R. Jaeschke Ubiergo, W. H. Campos, V. K. Bharadwaj, A. Chakraborty, *et al.*, *Nature Communications* **15**, 2116 (2024).
- [7] F. Zhang, X. Cheng, Z. Yin, C. Liu, L. Deng, Y. Qiao, Z. Shi, S. Zhang, J. Lin, Z. Liu, *et al.*, *Nature Physics* , 1 (2025).
- [8] B. Jiang, M. Hu, J. Bai, Z. Song, C. Mu, G. Qu, W. Li, W. Zhu, H. Pi, Z. Wei, *et al.*, *Nature Physics* , 1 (2025).
- [9] C. Wu, K. Sun, E. Fradkin, and S.-C. Zhang, *Physical Review B—Condensed Matter and Materials Physics* **75**, 115103 (2007).
- [10] L. Šmejkal, A. H. MacDonald, J. Sinova, S. Nakatsuji, and T. Jungwirth, *Nature Reviews Materials* **7**, 482 (2022).
- [11] M. Hu, X. Cheng, Z. Huang, and J. Liu, *Physical Review X* **15**, 021083 (2025).
- [12] Z. Zhou, X. Cheng, M. Hu, R. Chu, H. Bai, L. Han, J. Liu, F. Pan, and C. Song, *Nature* **638**, 645 (2025).
- [13] Y. Fang, J. Cano, and S. A. A. Ghorashi, *Physical Review Letters* **133**, 106701 (2024).
- [14] M. Ezawa, *Physical Review B* **110**, L241405 (2024).
- [15] Q. Ma, S.-Y. Xu, H. Shen, D. MacNeill, V. Fatemi, T.-R. Chang, A. M. Mier Valdivia, S. Wu, Z. Du, C.-H. Hsu, *et al.*, *Nature* **565**, 337 (2019).
- [16] S. Lai, H. Liu, Z. Zhang, J. Zhao, X. Feng, N. Wang, C. Tang, Y. Liu, K. Novoselov, S. A. Yang, *et al.*, *Nature Nanotechnology* **16**, 869 (2021).
- [17] A. Gao, Y.-F. Liu, J.-X. Qiu, B. Ghosh, T. V. Trevisan, Y. Onishi, C. Hu, T. Qian, H.-J. Tien, S.-W. Chen, *et al.*, *Science* **381**, 181 (2023).
- [18] N. Wang, D. Kaplan, Z. Zhang, T. Holder, N. Cao, A. Wang, X. Zhou, F. Zhou, Z. Jiang, C. Zhang, *et al.*, *Nature* **621**, 487 (2023).
- [19] S. Sankar, R. Liu, C.-P. Zhang, Q.-F. Li, C. Chen, X.-J. Gao, J. Zheng, Y.-H. Lin, K. Qian, R.-P. Yu,

- et al.*, Physical Review X **14**, 021046 (2024).
- [20] Z. Feng, X. Zhou, L. Šmejkal, L. Wu, Z. Zhu, H. Guo, R. González-Hernández, X. Wang, H. Yan, P. Qin, *et al.*, Nature Electronics **5**, 735 (2022).
- [21] R. Gonzalez Betancourt, J. Zubáč, R. Gonzalez-Hernandez, K. Geishendorf, Z. Šobáň, G. Springholz, K. Olejník, L. Šmejkal, J. Sinova, T. Jungwirth, *et al.*, Physical Review Letters **130**, 036702 (2023).
- [22] K. Kluczyk, K. Gas, M. Grzybowski, P. Skupiński, M. Borysiewicz, T. Fas, J. Suffczyński, J. Domagala, K. Grasza, A. Mycielski, *et al.*, Physical Review B **110**, 155201 (2024).
- [23] M. Chilcote, A. R. Mazza, Q. Lu, I. Gray, Q. Tian, Q. Deng, D. Moseley, A.-H. Chen, J. Lapano, J. S. Gardner, *et al.*, Advanced Functional Materials **34**, 2405829 (2024).
- [24] I. I. Mazin and K. Belashchenko, Physical Review B **110**, 214436 (2024).
- [25] A. Bose, N. J. Schreiber, R. Jain, D.-F. Shao, H. P. Nair, J. Sun, X. S. Zhang, D. A. Muller, E. Y. Tsymbal, D. G. Schlom, *et al.*, Nature Electronics **5**, 267 (2022).
- [26] H. Bai, L. Han, X. Feng, Y. Zhou, R. Su, Q. Wang, L. Liao, W. Zhu, X. Chen, F. Pan, *et al.*, Physical Review Letters **128**, 197202 (2022).
- [27] S. Karube, T. Tanaka, D. Sugawara, N. Kadoguchi, M. Kohda, and J. Nitta, Physical review letters **129**, 137201 (2022).
- [28] R. González-Hernández, L. Šmejkal, K. Výborný, Y. Yahagi, J. Sinova, T. Jungwirth, and J. Železný, Physical Review Letters **126**, 127701 (2021).
- [29] H. Bai, Y. Zhang, Y. Zhou, P. Chen, C. Wan, L. Han, W. Zhu, S. Liang, Y. Su, X. Han, *et al.*, Physical review letters **130**, 216701 (2023).
- [30] D.-F. Shao, Y.-Y. Jiang, J. Ding, S.-H. Zhang, Z.-A. Wang, R.-C. Xiao, G. Gurung, W. Lu, Y. Sun, and E. Y. Tsymbal, Physical Review Letters **130**, 216702 (2023).
- [31] X. Zhou, W. Feng, R.-W. Zhang, L. Šmejkal, J. Sinova, Y. Mokrousov, and Y. Yao, Physical review letters **132**, 056701 (2024).
- [32] A. Badura, W. H. Campos, V. K. Bharadwaj, I. Kounta, L. Michez, M. Petit, J. Rial, M. Leiviskä, V. Baltz, F. Krizek, *et al.*, Nature Communications **16**, 7111 (2025).
- [33] Z. Du, H.-Z. Lu, and X. Xie, Nature Reviews Physics **3**, 744 (2021).
- [34] W. Takei, D. E. Cox, and G. Shirane, Physical Review **129**, 2008 (1963).
- [35] A. Snow, Physical Review **85**, 365 (1952).
- [36] S. Abe, T. Kaneko, M. Ohashi, H. Yoshida, and K. Kamigaki, Journal of the Physical Society of Japan **53**, 2703 (1984).
- [37] W. Brinkman and R. J. Elliott, Proceedings of the Royal Society of London. Series A. Mathematical and Physical Sciences **294**, 343 (1966).
- [38] D. B. Litvin and W. Opechowski, Physica **76**, 538 (1974).
- [39] X. Chen, J. Ren, Y. Zhu, Y. Yu, A. Zhang, P. Liu, J. Li, Y. Liu, C. Li, and Q. Liu, Physical Review X **14**, 031038 (2024).
- [40] Y. Jiang, Z. Song, T. Zhu, Z. Fang, H. Weng, Z.-X. Liu, J. Yang, and C. Fang, Physical Review X **14**,

031039 (2024).

- [41] Z. Xiao, J. Zhao, Y. Li, R. Shindou, and Z.-D. Song, *Physical Review X* **14**, 031037 (2024).
- [42] G. Yang, Z. Li, S. Yang, J. Li, H. Zheng, W. Zhu, Z. Pan, Y. Xu, S. Cao, W. Zhao, *et al.*, *Nature Communications* **16**, 1442 (2025).
- [43] W. Lu, S. Feng, Y. Wang, D. Chen, Z. Lin, X. Liang, S. Liu, W. Feng, K. Yamagami, J. Liu, *et al.*, *Nano Letters* **25**, 7343 (2025).
- [44] Y. Gao, S. A. Yang, and Q. Niu, *Physical review letters* **112**, 166601 (2014).
- [45] I. Sodemann and L. Fu, *Physical review letters* **115**, 216806 (2015).
- [46] C.-P. Zhang, X.-J. Gao, Y.-M. Xie, H. C. Po, and K. T. Law, *Physical Review B* **107**, 115142 (2023).
- [47] J. Smit, *Physica* **21**, 877 (1955).
- [48] J. Smit, *Physica* **24**, 39 (1958).
- [49] C. Dames and G. Chen, *Review of scientific Instruments* **76** (2005).
- [50] Y. Tian, L. Ye, and X. Jin, *Physical review letters* **103**, 087206 (2009).
- [51] N. Nagaosa, J. Sinova, S. Onoda, A. H. MacDonald, and N. P. Ong, *Reviews of modern physics* **82**, 1539 (2010).
- [52] T. Urata, W. Hattori, and H. Ikuta, *Physical Review Materials* **8**, 084412 (2024).
- [53] P. Maker and R. Terhune, *Physical Review* **137**, A801 (1965).
- [54] R. Carman, R. Chiao, and P. Kelley, *Physical Review Letters* **17**, 1281 (1966).
- [55] N. Roch, E. Flurin, F. Nguyen, P. Morfin, P. Campagne-Ibarcq, M. H. Devoret, and B. Huard, *Physical review letters* **108**, 147701 (2012).
- [56] L. Min, Y. Zhang, Z. Xie, S. V. G. Ayyagari, L. Miao, Y. Onishi, S. H. Lee, Y. Wang, N. Alem, L. Fu, *et al.*, *Nature Materials* **23**, 1671 (2024).
- [57] Y. Kiyonaga, M. Mogi, R. Yoshimi, Y. Fujishiro, Y. Suzuki, M. T. Birch, A. Tsukazaki, M. Kawamura, M. Kawasaki, and Y. Tokura, *Advanced Materials* , e06210 (2025).
- [58] G. Kresse and J. Furthmüller, *Computational materials science* **6**, 15 (1996).
- [59] G. Kresse and J. Furthmüller, *Physical review B* **54**, 11169 (1996).
- [60] J. P. Perdew, K. Burke, and M. Ernzerhof, *Physical review letters* **77**, 3865 (1996).
- [61] A. A. Mostofi, J. R. Yates, Y.-S. Lee, I. Souza, D. Vanderbilt, and N. Marzari, *Computer physics communications* **178**, 685 (2008).

FIGURES

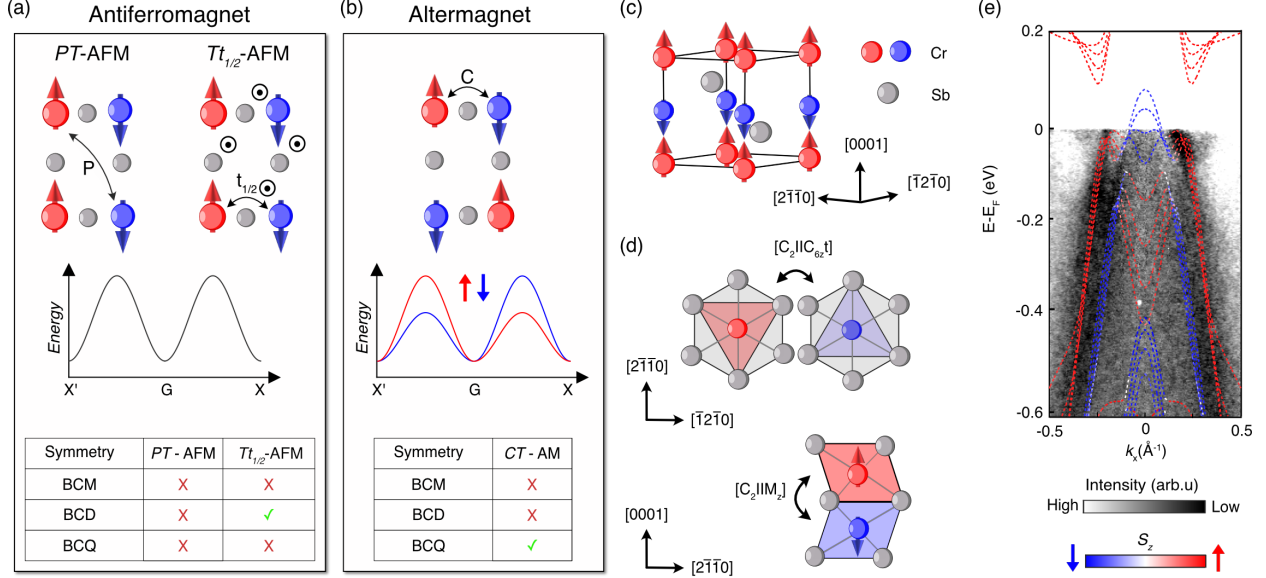


FIG. 1. **CrSb: a g-wave altermagnet.** (a) Top left: Shown is the lattice structure of a \mathcal{PT} -symmetric antiferromagnet, where the atomic sublattices are connected via inversion (\mathcal{P}) and time-reversal (\mathcal{T}) symmetry. Up and down spin orientations are color-coded in red and blue color, respectively. Top right: Shown is the lattice structure of a $t\mathcal{T}$ antiferromagnet, where the inversion is broken due to the presence of an extra grey atom out of the plane. Center: Shown is the schematics of the spin-degenerate electronic band structure of both \mathcal{PT} and $t\mathcal{T}$ antiferromagnets within the Brillouin zone. Bottom: The table illustrates which Berry curvature contributions are allowed (green check) and forbidden (red cross) to exist in antiferromagnets by symmetry arguments. BCM, BCD, and BCQ denote the Berry curvature monopole, dipole, and quadrupole, respectively. (b) Top: Shown is the illustration of the lattice structure of an altermagnet, schematically indicating the presence of C -symmetry operation to connect the two spin sublattices. Center: Shown is a schematic illustration of the spin-split electronic band structure of an altermagnet within the Brillouin zone. Bottom: The table illustrates which Berry curvature multipoles are allowed to exist in altermagnets by symmetry arguments. (c) Shown is the crystallographic and magnetic structure of CrSb. The Chromium (Cr) atoms with up-spin and down-spin are shown in red and blue color, respectively and antimony (Sb) atoms are shown as grey spheres. (d) Top: Shown are the anisotropic spin sublattices of CrSb connected via the combined symmetry rotation operation $[C_2^s \parallel C_{6z}t]$. Bottom: Shown are the anisotropic spin sublattices of CrSb connected via the mirror operation $[C_2^s \parallel M_z]$. (e) Shown is the momentum k_x and energy E -resolved angle-resolved photo-electron spectroscopy spectrum recorded on the surface of a cleaved CrSb crystal at $k_y = 3.3^{-1}$ and $k_z = 1.2^{-1}$ along a direction parallel to $\Gamma - K$ (see Methods section for details).

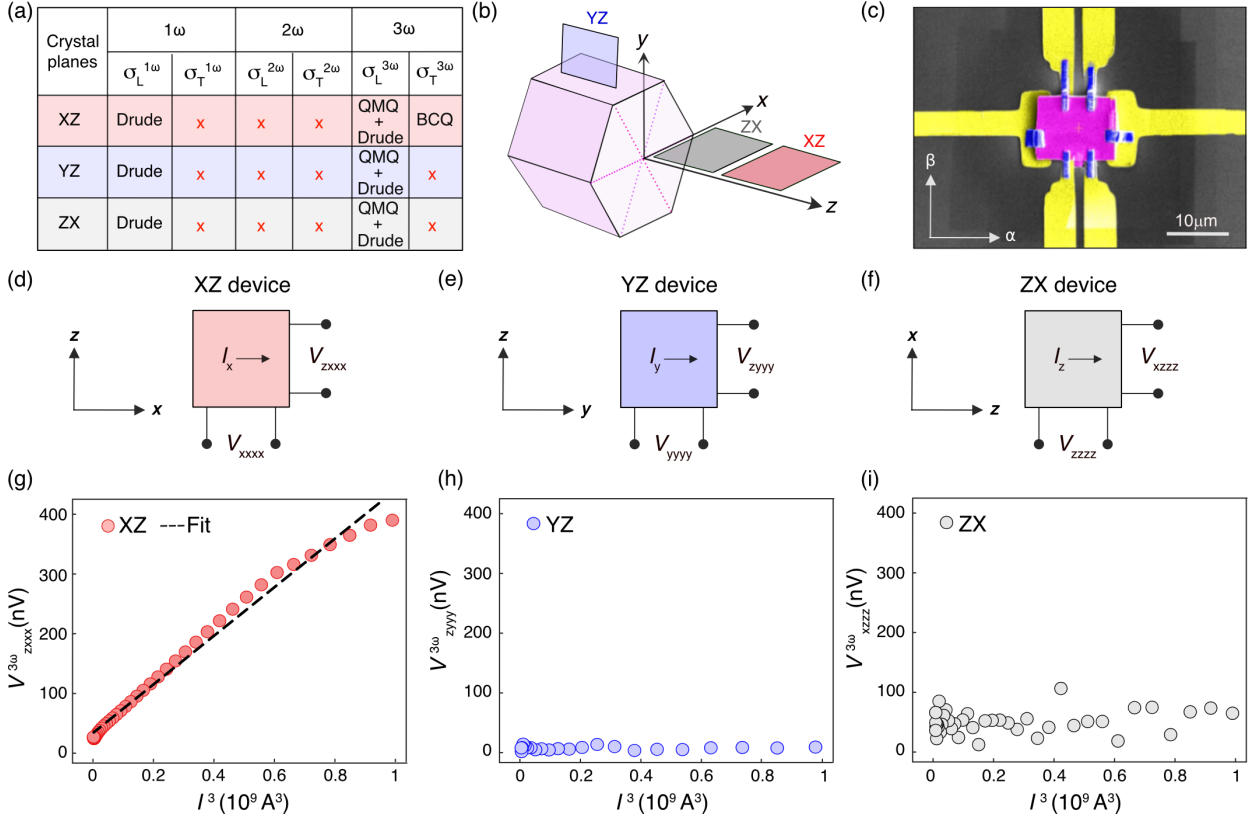


FIG. 2. Discovery of the third-order nonlinear anomalous Hall effect in altermagnetic CrSb at room temperature. (a) Shown is a summary of theoretically possible contributions—Drude scattering, quantum metric quadrupole (QM**Q**), and Berry curvature quadrupole (QM**Q**)—to the longitudinal ($\sigma_L^{n\omega}$) and transverse ($\sigma_T^{n\omega}$) linear (1ω) and nonlinear ($2\omega, 3\omega$) conductivities, respectively obtained from symmetry analysis within different crystallographic planes of CrSb. Red crosses indicate that contributions are prohibited by symmetry arguments. (b) Shown is a schematic illustration of the prism-shaped CrSb bulk crystal (light purple) as well as the spatial orientation of the lamellae ('XZ' red, 'YZ' blue, and 'ZX' grey) with respect to the bulk crystal. (c) Shown is a false-colored scanning electron microscopy image of the finished Hall bar device 'XZ' made from a crystalline lamella cut within the crystallographic xz -plane. The lamella, FIB-deposited Pt contacts, and prepatterned gold electrodes are highlighted by pink, blue, and yellow color, respectively. The SiO_2/Si substrate appears as black background. (d)-(f) Shown are schematic illustrations of the measurement geometry of the 'XZ', 'YZ', and 'ZX' devices, respectively. The bias current I_α and the longitudinal $V_{\alpha\alpha\alpha\alpha}$ and transverse $V_{\beta\alpha\alpha\alpha}$ voltage responses are denoted within the respective coordinate frame of each device. (g)-(i) Shown are the third-order nonlinear transverse voltage $V_{\beta\alpha\alpha\alpha}^{3\omega}$ as a function of the cubed bias current I_α^3 for the 'XZ' (red), 'YZ' (blue), and 'ZX' (grey) devices, respectively.

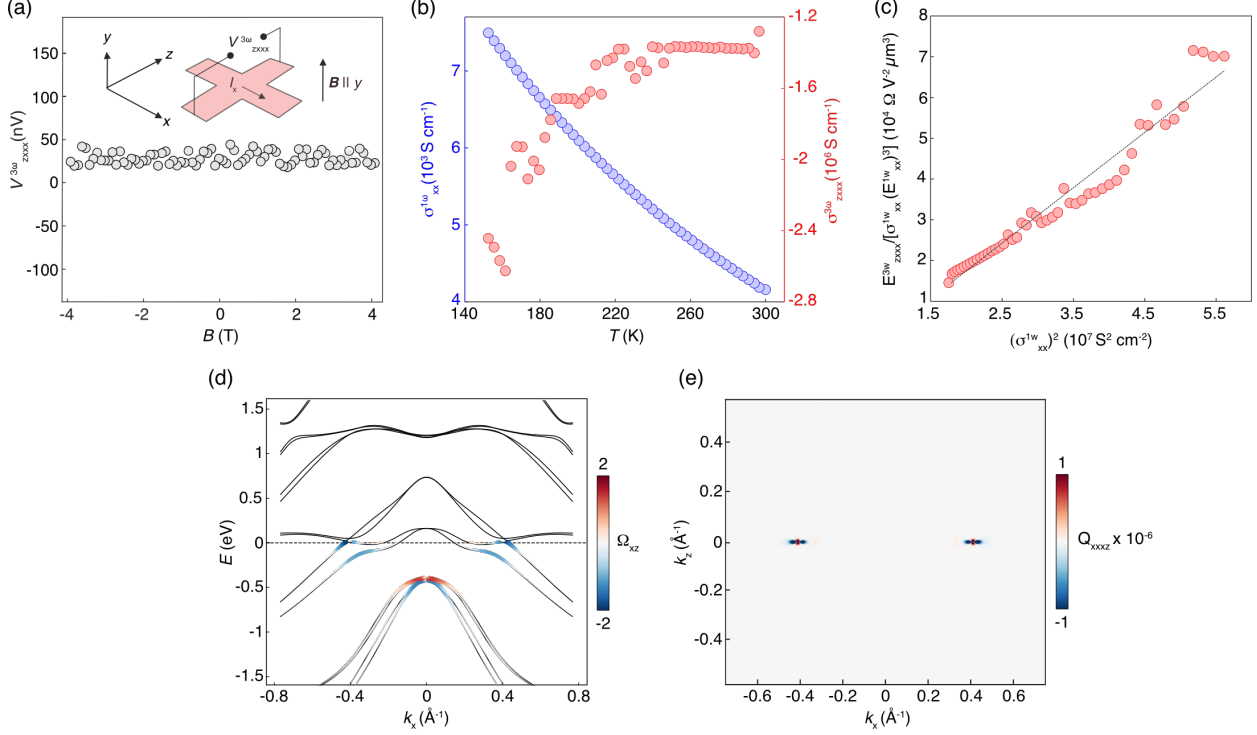


FIG. 3. Characterization of the third-order NLAHE of CrSb. (a) Shown is the third-order nonlinear transverse voltage $V_{zxxx}^{3\omega}$ as a function of an external magnetic field (B) applied along the y -direction. (b) Shown are the first-order longitudinal conductivity $\sigma_{xx}^{1\omega}$ (blue symbols) and the third-order transverse conductivity $\sigma_{zxxx}^{3\omega}$ (red symbols) as a function of temperature T . (c) Shown is $E_{zxxx}^{3\omega} / (\sigma_{xx}^{1\omega} (E_{xx}^{1\omega})^3)$ and fit to the data (dashed line) plotted as a function of the squared longitudinal conductivity $(\sigma_{xx}^{1\omega})^2$. (d) Shown is the electronic band structure of CrSb, as obtained from DFT calculations (see Methods section), overlaid with the amplitude of the Berry curvature Ω_{xz} . The band structure is plotted along the k_z direction at $k_y = 0$ and $k_z = 0.4 \text{ \AA}^{-1}$. (e) Shown is the momentum space distribution of Q_{zxxx} within the xz -plane of the Brillouin zone at Fermi energy.

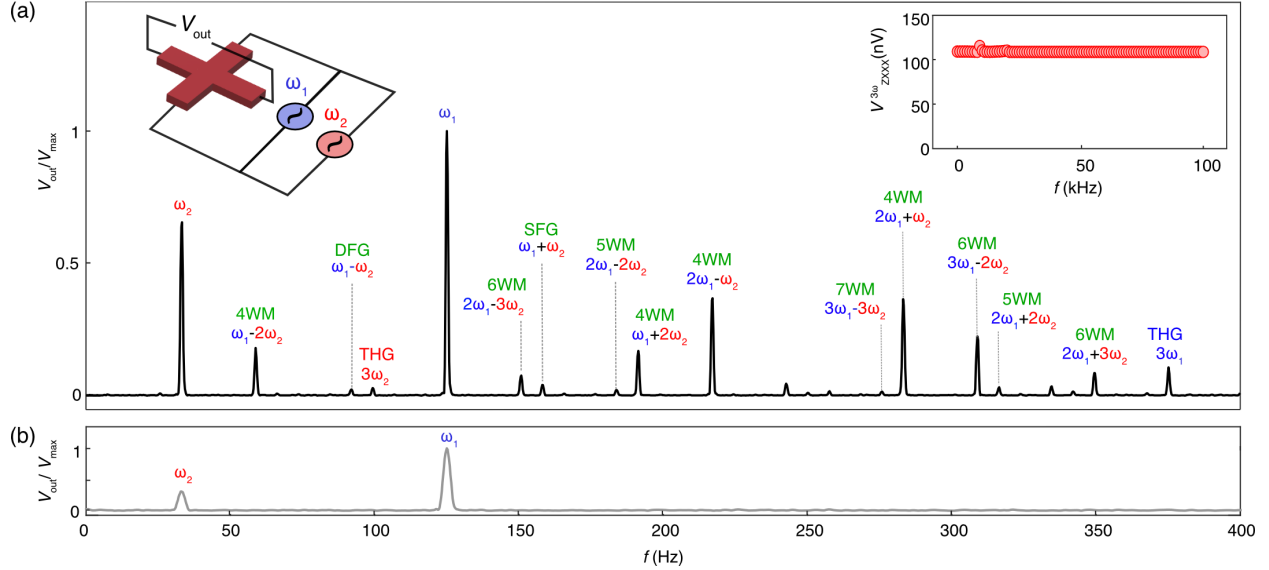
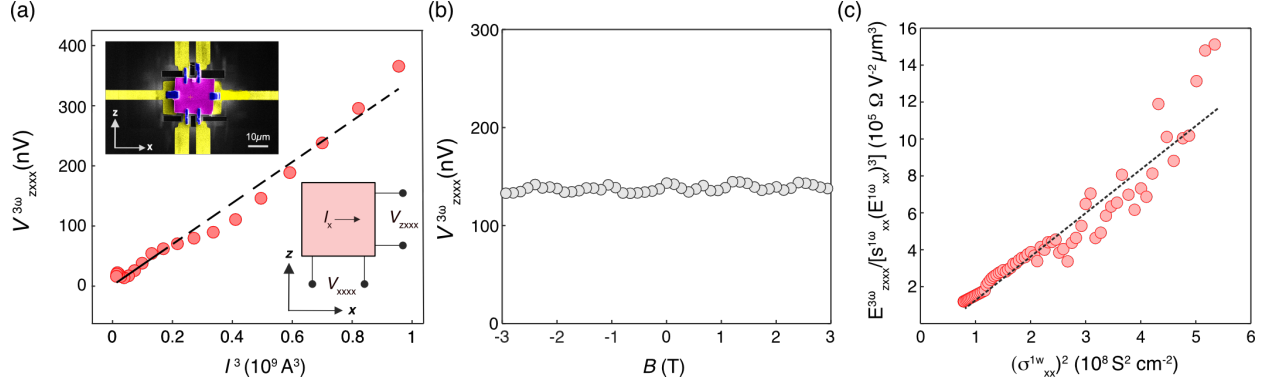
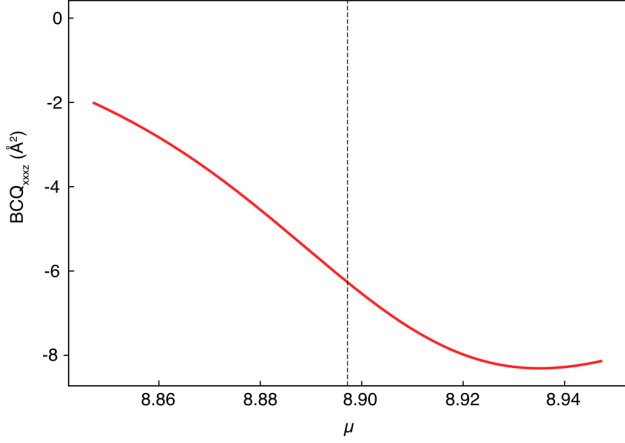


FIG. 4. Broadband multiple wave mixing in altermagnetic CrSb. (a) Shown is the frequency (f) spectrum of the output voltage V_{out} of a multiple wave mixer based on the 'XZ' device. V_{out} is normalized to the maximum output amplitude V_{max} seen at ω_1 . As schematically illustrated in the left inset two a.c. currents of different frequencies ($\omega_1 = 125$ Hz, $\omega_2 = 33$ Hz) were simultaneously applied to the 'XZ' Hall bar device and the frequency-dependent Hall voltage V_{out} was recorded. The detected output signals at different frequencies are labeled according to their origin, as described in the main text. The right inset displays the third-order nonlinear transverse voltage $V_{zxxx}^{3\omega}$ as a function of frequency $f = 0 - 100$ kHz of the longitudinal input current I_x . (b) Shown is the result of a control experiment where the frequency-dependent output voltage V_{out} was recorded when ω_1 and ω_2 are applied to a simple resistor with electric resistance $R = 100 \Omega$. V_{out} is normalized to the maximum output amplitude V_{max} seen at ω_1 .



Extended Data Figure 1. **Reproduction of the third-order NLAHE on device 'XZ2'.** We have fabricated another Hall bar device 'XZ2' from a CrSb lamella cut along the crystallographic xz -direction (see Methods section). (a) Shown is the third-order transverse voltage $V_{zxxx}^{3\omega}$ (circular symbols) recorded as a function of the cubed longitudinal bias current I_x at room temperature $T = 300$ K. The measurement geometry and a false colored scanning electric microscopy image of the device are shown as an inset. The linear fit (dashed line) to the data establishes the third-order nature of the detected signal. The amplitude of $V_{zxxx}^{3\omega}$ measured in device 'XZ2' quantitatively reproduces the amplitude of $V_{zxxx}^{3\omega}$ measured in device 'XZ'. (b) Shown is the magnetic field (B) dependence of $V_{zxxx}^{3\omega}$ at room temperature. Consistent with our observation on device 'XZ', $V_{zxxx}^{3\omega}$ is independent of the magnetic field amplitude over the examined field range. (c) Scaling law analysis of the third-order NLAHE. Shown is $E_{zxxx}^{3\omega} / (\sigma_{xx}^{1\omega} (E_{xx}^{1\omega})^3)$ (circular symbols) and linear fit to the data (dashed line) plotted as a function of the squared longitudinal conductivity $(\sigma_{xx}^{1\omega})^2$. From the fit, we extract a finite vertical intercept $\beta = (-106 \pm 3) \times 10^3 \Omega \mu\text{m}^3 \text{V}^{-2}$ and linear slope $\alpha = (2381 \pm 16) \times 10^{-6} \Omega^3 \mu\text{m}^5 \text{V}^{-2}$.



Extended Data Figure 2. **Finite Berry curvature quadrupole at Fermi energy from DFT calculations.** Shown is the momentum-space integrated Berry curvature quadrupole BCQ_{xxxx} plotted as a function of the chemical potential μ . The actual chemical potential of CrSb $\mu_0 = 8.8972\text{eV}$ is indicated by a vertical dashed line. The underlying Berry curvature distribution $Q_{xxxx}(k_x, k_z)$ in the xz -plane of the Brillouin zone is shown in Fig. 3(e). Details of the model calculation are presented in the Methods section.

METHODS

Crystal synthesis and characterization

Bulk single crystals of CrSb were grown by a flux method as described in detail elsewhere [52]. The obtained crystals are of hexagonal rod-like shape with typical dimensions of $0.2\text{ mm} \times 2\text{ mm}$ along the short and long axes, respectively. Out-of-plane X-ray diffraction and transmission Laue measurements confirmed the single-crystalline nature of the CrSb samples and revealed that the lateral facets correspond to the $\{01\bar{1}0\}$ planes, with the long axis parallel to the c -axis.

Microstructured device fabrication using FIB

Crystalline lamellas of CrSb for Hall bar device fabrication were prepared using an FEI Helios G4 UX Dual Beam FIB system. Thin lamellas of dimensions $20\text{ }\mu\text{m} \times 10\text{ }\mu\text{m} \times 2\text{ }\mu\text{m}$ were FIB-cut and extracted from the same piece of bulk CrSb single crystal along different crystallographic directions with an alignment accuracy of 0.5° to the respective crystallographic planes. The lamellae were then transferred to a copper grid using a platinum micromanipulator to perform thinning of the lamella and to remove an amorphous layer resulting from the FIB-cutting process using a low-voltage beam shower. Six-terminal Hall bars of dimensions $15\text{ }\mu\text{m} \times 8\text{ }\mu\text{m}$ were prepared on SiO_2/Si wafers of size $1\text{ cm} \times 1\text{ cm}$ followed by photolithography and $\text{Ti}(5\text{ nm})/\text{Au}(50\text{ nm})$ deposition using an e-beam evaporator. Each lamella was welded to the gold electrodes using Pt deposition with the FIB to prepare the final devices.

Electric transport measurements

All electric transport measurements were performed using a Quantum Design PPMS 6000 system using a four-probe contact geometry. The Hall bar devices were wire-bonded to the chip holder using $25\text{ }\mu\text{m}$ thick aluminum wire. An a.c. bias current of $I = I_0 \sin(\omega t)$ with a frequency of $f = \omega/2\pi = 19.375\text{ Hz}$ was applied by using an a.c. current source (6221A, Keithley). Unless otherwise noted, an amplitude of $I_0 = 0.6\text{ mA}$ was used. Three lock-in amplifiers (SRS 830, Stanford Research Systems), which are phase matched to the bias current output, were used to simultaneously record nonlinear longitudinal voltages $V_{\alpha\alpha}^{1\omega}$, $V_{\alpha\alpha\alpha}^{2\omega}$, $V_{\alpha\alpha\alpha\alpha}^{3\omega}$. Similarly, nonlinear transverse voltages $V_{\beta\alpha}^{1\omega}$, $V_{\beta\alpha\alpha}^{2\omega}$, and $V_{\beta\alpha\alpha\alpha}^{3\omega}$ were recorded simultaneously in a separate experimental run. Control experiments that confirm the accuracy of our lock-in detection scheme are presented in Sec. V of

the Suppl. Materials.

Angle-resolved photoelectron spectroscopy measurements

Conventional ARPES measurements were performed at the beamline UE112 PGM-2b-1² of BESSY (Berlin Electron Storage Ring Society for Synchrotron Radiation) synchrotron. The energy and angular resolutions were set to ≈ 20 meV and 0.3° , respectively, and the temperature was set to ≈ 20 K. The bulk crystalline samples for all ARPES measurements were cleaved *in situ* and measured in a vacuum better than 2×10^{-10} Torr.

Density Functional Theory calculation

Density functional theory (DFT) calculations of the electronic structure were performed using the density functional theory framework as implemented in the Vienna *ab initio* simulation package [58, 59]. The projector-augmented wave potential was adopted with the plane-wave energy cutoff set to 520 eV (convergence criteria 10^{-6} eV). The exchange-correlation functional of the Perdew–Burke–Ernzerhof type was used [60] with a $16 \times 16 \times 16$ gamma-centered Monkhorst–Pack mesh. We constructed the Hamiltonian of a Wannier tight-binding model using the *WANNIER90* interface [61], including the Cr *d*-and Sb *p*-orbitals. We then calculated the Berry curvature and quantum metric from this Wannier model using a $201 \times 201 \times 151$ k-mesh.

ACKNOWLEDGMENTS

The authors appreciate valuable discussions with Max Hirschberger and Shiming Lei. We also acknowledge the support of Siu Hin Kee for the sample fabrication using the focused ion beam method at the Materials Characterization and Preparation Facility at HKUST. This work was primarily supported by the Hong Kong Research Grant Council (Grant Nos. 26304221, 16302422, 16302624 awarded to BJ and C6033-22G awarded to BJ, JM, and JL), the Croucher Foundation (Grant No. CIA22SC02 awarded to BJ), and the National Key R&D Program of China (Grant No. 2021YFA1401500 awarded to JL). JL further acknowledges support from the Hong Kong Research Grants Council (Grant Nos. 16306722, 16304523, and C6046-24G). JM was supported by the National Natural Science Foundation of China (Grant No. 12422405), the Hong Kong Research Grants Council (Grant Nos. 21304023, C6033-22G, C1018-22E, C6046-24G, and C1002-24Y). TU was supported by Foundation of Public Interest of Tatematsu.

AUTHOR CONTRIBUTIONS

BJ, JL, and SS conceived the project. SS fabricated the FIB-cut Hall bar devices samples and conducted the electric transport measurements. Xingkai C, Xinyu C, and FX conducted the symmetry analysis and the model calculations and analyzed the data together with SS. Single crystals were grown by TU, WH, HI, CD, and CF. BJ, JL, and JM supervised the study. BJ wrote the manuscript with the input of all authors.

COMPETING INTEREST DECLARATION

The authors declare that they have no competing financial interest.

DATA AVAILABILITY STATEMENT

Replication data for this study can be accessed on Zenodo via the link XXX.